

## Revealing aggregation-induced emission effect of imidazolium derivatives and application for detection of Hg<sup>2+</sup>



Shuai Huang<sup>a</sup>, Tang Gao<sup>a</sup>, Anyao Bi<sup>a</sup>, Xiaozheng Cao<sup>a</sup>, Bin Feng<sup>a</sup>, Min Liu<sup>a</sup>, Tao Du<sup>b</sup>, Xueping Feng<sup>b</sup>, Wenbin Zeng<sup>a,\*</sup>

<sup>a</sup> Xiangya School of Pharmaceutical Sciences, Central South University, Changsha, 410013, PR China

<sup>b</sup> Xiangya Hospital, Central South University, Changsha, 410013, PR China

### ARTICLE INFO

#### Keywords:

Aggregation-induced emission (AIE)  
Conformation function group (CFG)  
Restriction of intramolecular rotations (RIR)  
Coplanarity  
Fluorescent probe  
Mercury bioimaging

### ABSTRACT

Despite being highly emissive in solution, aggregation of 4-(4,5-bis(4-methoxyphenyl)-1H-imidazole-2-yl) benzaldehyde (**BMI**) molecules typically results in the quenching of fluorescence. To overcome the shortcomings of aggregation-caused quenching (ACQ), the substituent of imidazole in the nitrogen atom of the **BMI** has been found as a conformation function group (CFG) to turn the aggregation-induced emission (AIE) effect. The introduction of CFG not only causes the restriction of intramolecular rotations (RIR) effect, but also attenuates the coplanarity of the molecule. As a result, the **BMI** with ACQ effect is transformed into **BMI**s with AIE effect. As the steric hindrance of the CFG increases, the AIE characteristic of the derivative also becomes apparent. With the assistance of the thioacetal unit, **BMIBD** can act as an outstanding probe for the detection of Hg<sup>2+</sup> with high sensitivity and selectivity. A series of characterizations were implemented to prove the unique response mechanism of **BMIBD** toward mercury ions, including optical behavior investigation, mass analysis and <sup>1</sup>H NMR studies. Further, the detection limit is low up to 36 nM. Taking advantages of excellent optical properties of this AIE probe **BMIBD**, point-of-care testing (POCT) for Hg<sup>2+</sup> detection was further investigated. Meanwhile, **BMIBD** presented the desirable analytical property for the real water samples. Additionally, cellular imaging experiment revealed that the probe has an excellent biocompatibility that could be applied for tracking Hg<sup>2+</sup> in living cells.

### 1. Introduction

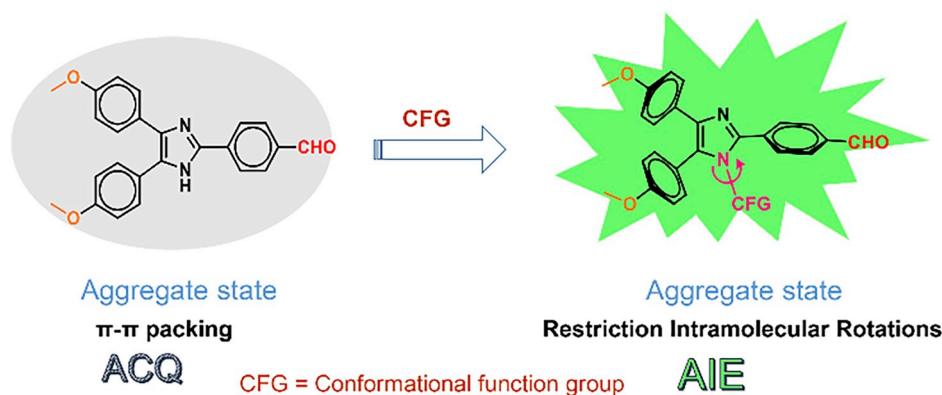
Due to its simplicity, high sensitivity and capability of real-time and non-invasive fluorescent imaging, fluorescence detection of small molecules and biomacromolecules has attracted widespread attention [1,2]. It is well known that the detection of biomolecules or other species in the cell are often performed in aquatic environment [3]. However, the conventional fluorophores (such as fluorescein, rhodamine, and cyanine) are prone to aggregation in the water-soluble environment, resulting in fluorescence quenching [4–8]. The aggregation-caused quenching (ACQ) greatly limits its practical application in physiological environment [9–12]. Fortunately, with the discovery of aggregation-induced emission (AIE), new opportunities to overcome the ACQ effect have emerged [13–15]. In contrast to ACQ, fluorescent molecules with AIE effect emit intensely in the aggregates while showing barely no fluorescence in a dilute solution [16]. Up to now, various mechanisms have been proposed to elucidate the mechanistic causes for the AIE phenomena, including restriction of intramolecular rotations (RIR), J-aggregate formation, conformational planarization,

twisted intramolecular charge transfer (TICT), E/Z isomerization, and excited state intramolecular proton transfer (ESIPT) [17–19]. As one of the main hypotheses, the RIR process inhibits the free vibration and rotation of the molecule, reducing the energy consumed, thereby consuming energy through the path of radiation, ultimately resulting in fluorescence emission [20,21]. Although a variety of strategies of transforming fluorophores of ACQ into AIE groups have been illustrated, the role of RIR and coplanarity in the AIE characteristics is still undetermined and its universality subjects to further verification [22–24].

In our previous work, we successfully constructed a series of tetra-aryl imidazole derivatives with AIE characteristics [25,26]. Compare to tetra-aryl imidazole derivatives, the triaryl imidazole derivatives exhibit typically ACQ effect. In consideration into the mechanism of RIR, we hypothesized that introducing a branched chain or bulky ring to the nitrogen on the imidazole ring could endow the triaryl imidazole with AIE effect. Besides the RIR effect, the substitution at the N position may also affect the molecular planarity, resulting in less possibility of  $\pi$ - $\pi$  stacking in the process of aggregates (see Scheme 1). Herein, a series of

\* Corresponding author.

E-mail address: [wbzeng@hotmail.com](mailto:wbzeng@hotmail.com) (W. Zeng).



**Scheme 1.** Conversion strategy from ACQ fluorophores to AIE fluorophores by introducing a CFG.

modified triaryl imidazole fluorophores were synthesized and exhibited excellent AIE characteristics. This strategy may not only provide a solid proof for the mechanism of RIR, but also offer a new avenue to design novel AIE-based fluorophores. Besides, some probes for mercury detection have been reported [27–29]. Among those modification for molecular probe, 2-mercaptoethanol is a specific site for mercury ion detection after its condensation with an aldehyde group, simultaneously increases the probe's water solubility. Here, after the detailed screening, **BMIB** was selected and applied for the detection of mercury ions.

As a highly toxic heavy metal and highly ubiquitous contaminant [30–33], mercury in elemental and ionic form could be engulfed from the unpurified water [34–36]. It could also be assimilated through the food chain when it is converted into methylmercury by the bacterial transformation [37]. Excessive accumulation of mercury in the body may seriously endanger human health, and do harm to extensive organs and tissues, including heart, kidney, brain and nervous system [38–40]. Moreover, methylmercury and mercuric chloride are also considered the possible carcinogen [41–43]. Therefore, it is necessary to develop useful fluorescent probe to detect mercury in biological systems and ecological environments [44–46].

As known, the presence of trace amount of mercury ions would induce the umpolung reaction on the triaryl imidazole-based acyclic thioacetals. As a result, **BMIB** having an aldehyde group is produced and aggregated into nanoparticles in an aqueous solution. Which causes the enhanced fluorescence emission via strengthening electronic push-pull effect and aggregation from the dissolved state. A series of characterizations were implemented to prove the unique response mechanism of **BMIBD** toward mercury ions, including optical behavior investigation, mass analysis and  $^1\text{H}$  NMR studies. These experiments have shown that **BMIBD** can act as a superior sensor for  $\text{Hg}^{2+}$  which possesses high selectivity and sensitivity. Moreover, **BMIBD** was applied to the thin film and further used for  $\text{Hg}^{2+}$  detection. Meanwhile, **BMIBD** showed desirable analytical properties in real water. Additionally, cellular imaging experiment revealed that **BMIBD** could be applied for tracking mercury ion in living cells with excellent biocompatibility.

## 2. Experimental section

### 2.1. Materials and instruments

All inorganic salts, NaCl,  $\text{CaCl}_2$ ,  $\text{FeCl}_2$ ,  $\text{CoCl}_2$ ,  $\text{Cd}(\text{NO}_3)_2$ ,  $\text{Al}(\text{NO}_3)_3$ ,  $\text{MnCl}_2$ ,  $\text{AgNO}_3$ ,  $\text{FeCl}_3$ ,  $\text{CrCl}_2$ , KCl,  $\text{Mg}(\text{NO}_3)_2$ ,  $\text{ZnCl}_2$ , and  $\text{HgCl}_2$ , were purchased from Sinopharm Chemical Reagent Co., Ltd. (China). *p*-Anisil was purchased from Nine-Dinn Chemistry (Shanghai) Co., Ltd. 1,4-Phthalaldehyde was purchased from Energy Chemical Co., Ltd (China). Benzylamine was purchased from Sionpharm Chemical Reagent Co., Ltd. Iodomethane was purchased from Xiya Chemical Industry Co., Ltd

(Shandong). Bromoethane was purchased from Tianjin Guangfu Fine Chemical Research Institute. Silica gel (200–300 mesh) was purchased from Qingdao Ocean Chemicals (Qingdao, China). 2-Mercapto-ethanol was purchased from Aladdin Company (Shanghai, China).  $^1\text{H}$  and  $^{13}\text{C}$  NMR spectra were measured on a Bruker ARX 500 MHz NMR and 125 MHz respectively. The pH was validated employing a Lei Ci PHS-3C pH meter. HPLC analysis was carried on by using Shimadzu LC-20AD. Fluorescent spectra were recorded on a Shimadzu RF-5301.

### 2.2. Synthesis of BMI

Compound **2** was synthesized according to our method [22]. Compound **2** (810 mg, 3 mmol) and 1,4-phthalaldehyde (402 mg, 3 mmol) were dissolved in acetic acid (10 mL) followed stirring for 5 h at 120 °C. The obtained reaction system was extracted with ethyl acetate and purified by column chromatography. The final product **BMI** (645 mg, 56%) was obtained as a pale yellow solid.  $^1\text{H}$  NMR (500 MHz,  $\text{CDCl}_3$ )  $\delta$  10.01 (s, 1H), 8.08 (d,  $J = 7.4$  Hz, 2H), 7.91 (d,  $J = 7.6$  Hz, 2H), 7.46 (d,  $J = 7.5$  Hz, 4H), 6.88 (d,  $J = 8.0$  Hz, 4H), 3.83 (s, 6H).  $^{13}\text{C}$  NMR (125 MHz,  $\text{CDCl}_3$ )  $\delta$  191.92, 159.10, 144.02, 135.47, 135.30, 133.53, 130.28, 129.19, 125.47, 124.82, 114.01, 55.27. HRMS: calcd for  $[\text{M} + \text{H}]^+$ : 385.1507; found: 385.1571.

### 2.3. Synthesis of BMIM

**BMI** (384 mg, 1 mmol) and sodium hydride (48 mg, 2 mmol) were dissolved in anhydrous DMF (5 mL) and stirred at 60 °C for 1 h under the protection of nitrogen, then iodomethane (142 mg, 1 mmol) was added and the reaction system was stirred for 3 h at 90 °C. The reaction system was extracted with ethyl acetate, dried over anhydrous magnesium sulfate, and dried by vacuum. The crude product was purified by the chromatographic column to yield a yellow solid 4-(4,5-bis(4-methoxyphenyl)-1-methyl-1H-imidazole-2-yl)benzaldehyde (**BMIM**) (207 mg, 52%).  $^1\text{H}$  NMR (500 MHz,  $\text{CDCl}_3$ ) 10.08 (s, 1H), 7.99 (dd,  $J = 19.1$ , 8.0 Hz, 4H), 7.50 (d,  $J = 8.4$  Hz, 2H), 7.33 (d,  $J = 8.3$  Hz, 2H), 7.03 (d,  $J = 8.3$  Hz, 2H), 6.80 (d,  $J = 8.5$  Hz, 2H), 3.89 (s, 3H), 3.78 (s, 3H), 3.56 (s, 3H).  $^{13}\text{C}$  NMR (125 MHz,  $\text{CDCl}_3$ ) 191.42, 160.04, 158.12, 145.64, 138.10, 136.52, 135.67, 130.65, 129.91, 129.89, 129.17, 127.90, 126.79, 122.64, 114.25, 113.28, 54.96, 33.20, 29.25. HRMS: calcd for  $[\text{M} + \text{H}]^+$ : 399.1664; found: 399.1708.

### 2.4. Synthesis of BMIE and BMIB

4-(1-Ethyl-4,5-bis(4-methoxyphenyl)-1H-imidazole-2-yl)benzaldehyde (**BMIE**) and 4-(1-benzyl-4,5-bis(4-methoxyphenyl)-1H-imidazole-2-yl)benzaldehyde (**BMIB**) were synthesized in the light of the general procedure of **BMIM**. **BMIE** (Yellow solid, 54%)  $^1\text{H}$  NMR (500 MHz,  $\text{CDCl}_3$ ) 10.10 (s, 1H), 8.01 (s, 2H), 7.94 (d,  $J = 7.6$  Hz, 2H), 7.48 (d,  $J = 7.7$  Hz, 2H), 7.35 (d,  $J = 7.6$  Hz, 2H), 7.05 (d,  $J = 7.6$  Hz, 2H), 6.79

(d,  $J = 7.8$  Hz, 2H), 4.00 (d,  $J = 7.1$  Hz, 2H), 3.91 (s, 3H), 3.78 (s, 3H), 1.09 (t,  $J = 7.0$  Hz, 3H).  $^{13}\text{C}$  NMR (125 MHz,  $\text{CDCl}_3$ ) 191.70, 160.00, 158.36, 145.25, 138.44, 137.11, 135.99, 132.33, 129.96, 129.47, 129.32, 127.92, 127.03, 123.12, 114.63, 113.60, 54.96, 39.47, 29.56, 16.06. HRMS: calcd for  $[\text{M} + \text{H}]^+$ : 413.1820; found: 413.1883.

**BMIB** (Yellow solid, 49%)  $^1\text{H}$  NMR (500 MHz,  $\text{CDCl}_3$ ) 10.03 (s, 1H), 7.89 (dd,  $J = 17.1$ , 8.0 Hz, 4H), 7.54 (d,  $J = 8.4$  Hz, 2H), 7.26 (d,  $J = 7.1$  Hz, 3H), 7.15 (d,  $J = 8.2$  Hz, 2H), 6.88 (d,  $J = 7.6$  Hz, 4H), 6.80 (d,  $J = 8.4$  Hz, 2H), 5.15 (s, 2H), 3.83 (s, 3H), 3.79 (s, 3H).  $^{13}\text{C}$  NMR (125 MHz,  $\text{CDCl}_3$ ) 191.64, 162.51, 160.00, 158.53, 145.91, 138.49, 137.75, 137.23, 135.99, 132.34, 130.18, 129.88, 129.19, 128.82, 128.01, 127.62, 125.82, 122.49, 114.42, 113.66, 55.25, 55.18, 48.43. HRMS: calcd for  $[\text{M} + \text{H}]^+$ : 475.1977; found: 475.2047.

## 2.5. Synthesis of CBMIB

Terephthalaldehyde (134 mg, 1 mmol) and 4-chloroaniline (127 mg, 1 mmol) were dissolved in ethanoic acid (15 mL) followed stirring for 1 h at 25 °C. Compound **2** (270 mg, 1 mmol) and ammonium acetate (540 mg, 7 mmol) were added subsequently. The mixture was heated at 120 °C overnight. After quenching with water, the mixture was adjusted to neutral, extracted with ethyl acetate, dried over anhydrous magnesium sulfate and dried in vacuo. Purify the crude product by column to obtain 4-(1-(4-chlorophenyl)-4,5-bis(4-methoxyphenyl)-1H-imidazole-2-yl)benzaldehyde (**CBMIB**) as a pale yellow solid (207 mg, 42%).  $^1\text{H}$  NMR (500 MHz,  $\text{CDCl}_3$ )  $\delta$  9.98 (s, 1H), 7.79 (d,  $J = 8.3$  Hz, 2H), 7.61 (d,  $J = 8.3$  Hz, 2H), 7.56–7.52 (m, 2H), 7.29 (dd,  $J = 6.6$ , 2.0 Hz, 2H), 7.07–7.04 (m, 2H), 7.02–6.98 (m, 2H), 6.84–6.80 (m, 4H), 3.81 (s, 3H), 3.80 (s, 3H).  $^{13}\text{C}$  NMR (125 MHz,  $\text{CDCl}_3$ )  $\delta$  191.69, 159.52, 158.68, 144.91, 138.93, 135.89, 135.52, 135.49, 134.59, 132.34, 130.87, 129.64, 129.58, 129.55, 129.07, 128.43, 126.64, 122.06, 114.14, 113.73, 55.21, 55.18. HRMS: calcd for  $[\text{M} + \text{H}]^+$ : 495.1431; found: 495.1491.

## 2.6. Synthesis of BMIBD

**BMIB** (237 mg, 0.5 mmol) was dissolved in 5 mL absolute ethanol, p-toluene sulfonic acid and 2-mercaptoethanol (79 mg, 1 mmol) was added followed stirring for 6 h under the protection of nitrogen at 80 °C. Subsequently the solvent was removed and the mixture was separated by the high-performance liquid chromatography to afford 2,2'-((4-(1-benzyl-4,5-bis(4-methoxyphenyl)-1H-imidazole-2-yl)phenyl)methylene)bis(sulfanediy)bis(ethan-1-ol) (**BMIBD**) as pale white solid (187 mg, 61%).  $^1\text{H}$  NMR (500 MHz,  $\text{DMSO}-d_6$ ) 7.78 (d,  $J = 7.7$  Hz, 2H), 7.65 (d,  $J = 7.7$  Hz, 2H), 7.39 (d,  $J = 7.9$  Hz, 2H), 7.31 (d,  $J = 7.8$  Hz, 2H), 7.20 (s, 3H), 7.03 (d,  $J = 7.8$  Hz, 2H), 6.96 (d,  $J = 8.0$  Hz, 2H), 6.83 (d,  $J = 4.1$  Hz, 2H), 5.37 (s, 1H), 5.26 (s, 2H), 3.79 (s, 3H), 3.75 (s, 3H), 3.54 (t,  $J = 6.6$  Hz, 4H), 2.71–2.66 (m, 2H), 2.57 (dd,  $J = 13.2$ , 6.6 Hz, 2H).  $^{13}\text{C}$  NMR (125 MHz,  $\text{DMSO}-d_6$ ) 160.83, 160.01, 145.29, 144.70, 139.86, 135.52, 132.93, 131.52, 130.16, 130.09, 129.08, 128.66, 128.26, 126.75, 124.05, 119.19, 117.94, 115.21, 114.63, 60.85, 55.26, 51.97, 48.70, 34.85, 31.57. HRMS: calcd for  $[\text{M} + \text{H}]^+$ : 613.2150; found: 613.2157.

## 2.7. General procedure for the spectra measurement

The stock solutions of  $\text{Na}^+$ ,  $\text{Ca}^{2+}$ ,  $\text{Fe}^{2+}$ ,  $\text{Al}^{3+}$ ,  $\text{Mn}^{2+}$ ,  $\text{Ag}^+$ ,  $\text{Fe}^{3+}$ ,  $\text{Cr}^{3+}$ ,  $\text{Cd}^{2+}$ ,  $\text{K}^+$ ,  $\text{Mg}^{2+}$ ,  $\text{Zn}^{2+}$  and  $\text{Co}^{2+}$  were prepared in deionized water and were first configured as a 10 mmol. First prepared 1 mM of **BMIBD** solution in DMSO, then diluted to 10  $\mu\text{M}$  using PBS (10 mM, pH 7.4). Then 10  $\mu\text{L}$  of different ion solution, 980  $\mu\text{L}$  of PBS and 10  $\mu\text{L}$  of **BMIBD** were configured as a 1 mL solution. The **BMIBD** solution (1 mM) of 10  $\mu\text{L}$  was taken from the pipette gun and added to the PBS buffer containing different  $\text{Hg}^{2+}$  concentration at 990  $\mu\text{L}$ . To study the practical application of **BMIBD** for detecting mercury ions, a real water sample from Xiangjiang River was collected. The water sample was

filtered through a 0.22  $\mu\text{m}$  membrane and configured into samples of different mercury ion concentrations. Later, 10  $\mu\text{L}$  of **BMIBD** (1 mM) was added to 990  $\mu\text{L}$  of the samples individually. All samples were measured after incubation at 37 °C for 30 min and then the fluorescence spectra were recorded using 380 nm as the excitation wavelength.

## 2.8. Fluorescence imaging of $\text{Hg}^{2+}$ in living cells

MDA-MB-231 cells were incubated at 37 °C in Dulbecco's modified Eagle medium (DMEM) supplemented with 10% fetal bovine serum (FBS), 100 IU/mL penicillin and 100  $\mu\text{g}/\text{mL}$  streptomycin in a humidified incubator containing 5%  $\text{CO}_2$ . Cells were treated with mercury chloride (5  $\mu\text{M}$  or 10  $\mu\text{M}$ ) in DMEM for 1 h at 37 °C, and then washed several times with PBS in order to remove the free  $\text{Hg}^{2+}$  ions. **BMIBD** was incubated in the cell medium for 30 min, then washed the media with PBS. The fluorescence imaging of  $\text{Hg}^{2+}$  in living cells on the slide was observed by confocal fluorescence microscope following addition of 50% glycerol.

## 3. Results and discussion

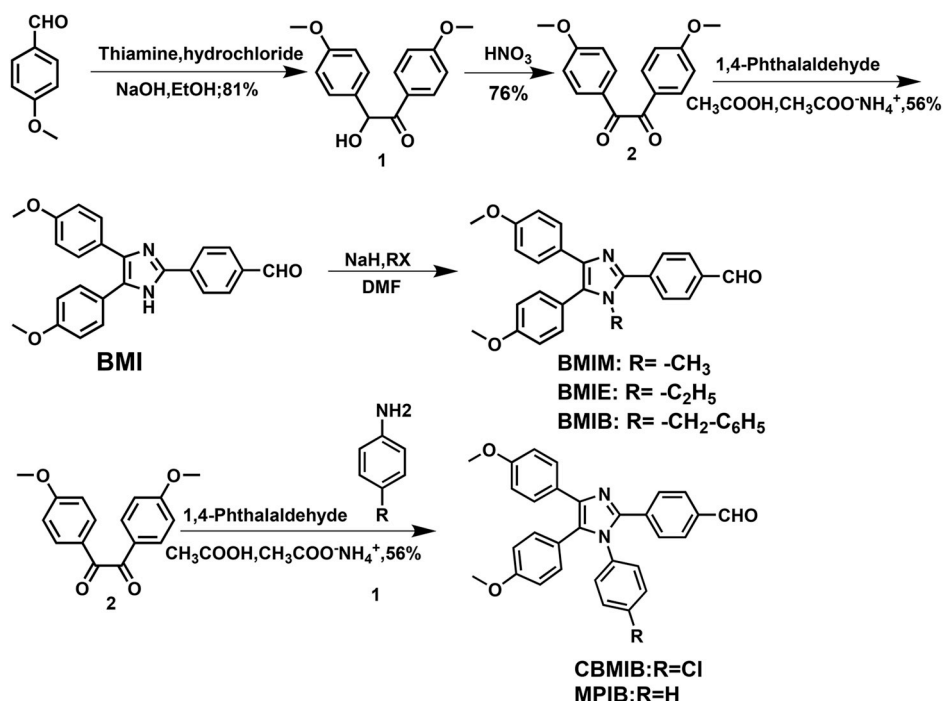
### 3.1. Design and synthesis

With **BMI** in hand, we explored how the different substituents as conformation functional groups to affect the AIE properties of **BMI**s. The synthetic routes were shown in Scheme 2. All of these products have been confirmed by  $^1\text{H}$ NMR,  $^{13}\text{C}$ NMR, and **BMIBD** has been further confirmed by mass spectrum.

### 3.2. Photophysical properties of BMI derivatives

First, the optical properties of these derivatives were investigated. It was observed that fluorescence emission of these compounds was red-shifted with a decreased tendency in intensity if the polarity of the solvent increased (Fig. S1). To further verify the ICT mechanism, density functional theory was implemented to calculate the electron cloud distributions of these derivatives ((B3LYP level of theory, 6-31G (d3, 3p) basis set). As shown in Fig. 1, the electronic clouds in the HOMO orbitals of these molecules were largely allocated on the electron donating groups, while in the LUMO orbitals, the electron clouds were mainly distributed in the electron withdrawing groups. These results coincided with the characteristics of the ICT effect, thus further demonstrating that these molecules possess ICT effect. As a comparison, the electronic cloud distribution of the probe **BMIBD** appeared to be more dispersed, thus its ICT effect was weaker than other **BMI** derivatives. Additionally, from their most stable conformation, it could be observed that as the steric hindrance of imidazole group increased, the coplanarity of the entire molecule gradually weakened.

Followed, the AIE effect of these derivatives were investigated. They showed good solubility in DMSO, but not in water. Therefore, different DMSO/water systems were selected as the measurement system of the AIE effect. As can be seen from Fig. 2b, with the water ratio elevated from 10% to 50%, the fluorescence intensity of **BMI** attenuated rapidly, and the fluorescence was substantially quenched when the water ratio was 50%. Obviously, **BMI** is a typical ACQ fluorophore. Similarly, **BMIM** showed an obvious solvent effect. As the polarity of solvents increased, fluorescence emission of **BMIM** red-shifted with a decreased in intensity, as shown in Fig. S1f. Additionally, the AIE effect of **BMIM** was also studied. The fluorescence intensity of **BMIM** decreased when the water ratio was 10%–40% and remained unchanged between 40% and 90%. However, when the water ratio reached 99%, the fluorescence intensity had no obvious change. It indicated that **BMIM** has a weak AIE effect. On the other hand, we examined whether **BMIE** has the AIE effect. When the water ratio was lower than 80%, the fluorescence intensity of **BMIE** was very weak (Fig. 2f). Upon the water ratio was higher than 80%, the fluorescence intensity increased rapidly and



Scheme 2. The synthetic route of BMI and derivatives.

reached the highest when the water ratio was increased to 99%.

In Fig. 2g, with the water contents increased from 10% to 20%, we found the fluorescent intensity of **BMIB** decreased and the emission wavelength appeared red-shift. This change was ascribed to the enhancement in the ICT effect owing to the increased water content led to an increase in the polarity of the solution. Upon increasing the polarity of the solvent, the fluorescent emission wavelength of **BMIB** red-shifted, and the fluorescence quantum yield reduced, which was consistent with the ICT effect [47]. With the increased water fractions from 20% to 50%, the fluorescent emission of **BMIB** was quenched gradually, indicating that the fluorescence intensity of **BMIB** was decided by the ICT effect, but not the RIR process. In a sharp contrast, when the water contents were elevated from 50% to 99%, the intensity of fluorescence enhanced (16-fold), while the fluorescence maximum emission blue-shifted from 530 nm to 495 nm. The properties of **CBMIB** were depicted as shown in Fig. 2i. **CBMIB** emitted nearly no fluorescence when the water content in the solvent was less than 60%. While the water fraction was in the extent of 60%–80%, the fluorescent emission of **CBMIB** increased. Interesting, **CBMIB** showed an obvious AIE phenomenon when the water content was between 80% and 99%. Furthermore, according to our previous works [25], the nitrogen atom of the imidazole ring substituted with a benzene ring have exhibited excellent AIE effect (Fig. S2). Therefore, we speculated that substituent of imidazole in the nitrogen atom of **BMI** may be as a conformation function group (CFG) to turn the AIE effect.

Base on the above results, it suggested that the steric hindrance plays a crucial role for their AIE characteristics. When the substituent in **BMI** was hydrogen, the steric hindrance was too small to affect the coplanarity. Thus, **BMI** showed an ACQ effect owing to the  $\pi$ - $\pi$  stacking. But concerning **BMIM** or **BMIE** whose CFG was methyl or ethyl, the role of steric hindrance appears. These types of alkyl chains not only affect the coplanarity of the molecules, but also could facilitate the restriction of intramolecular rotation in the aggregates. Such a device greatly reduced the energy consumed by the vibration and rotation of the molecule, thus strong fluorescence emission in aggregation state, namely AIE Effect, is observed. Regrettably, due to the small steric hindrance, methyl group has weak ability to limit intramolecular rotation, resulting in **BMIE** showing weak AIE effect. On the contrary,

the larger CFG such as benzene ring and benzyl group not only restricted the free rotation in the molecule, but also destroyed the coplanarity of molecules. So, the AIE effect of **BMIB** and **CBMIB** presented more obviously. Importantly, the different ability of the benzyl group and benzene ring to modulate the AIE properties was examined as shown in Fig. 2. The AIE effect of **CBMIB** started from the water content of 70% while **BMIB** was from 50%. Due to its greater steric hindrance, the benzyl group showed higher potency in AIE effect without the requirement of a very concentrated state. These results further illustrated the role of steric hindrance provided by CFG in the AIE effect.

From these comparative experiments depicted above, it was revealed that **BMIB** exhibited excellent AIE characteristic. Next, we explored its application in chemical sensor and fluorescent imaging. It is reported that 2-mercaptoethanol can not only be used as a specific target for mercury ion detection after condensation with an aldehyde group, but also increase the water solubility of the probe. Taking above in mind, we designed and synthesized fluorescent probe **BMIBD** for detection of mercury ion. **BMIBD** was obtained from the reaction of **BMIB** with 2-mercaptoethanol (Scheme S1). After the response to the mercury, the umpolung of the probe led to fluorescence emission, meanwhile the fluorescence signal was further amplified by the AIE effect due to the aggregation of **BMIB** with worse solubility.

### 3.3. Fluorescence response to Hg<sup>2+</sup>

The fluorescence responsive behaviour of **BMIBD** toward Hg<sup>2+</sup> were explored in PBS buffer (10 mM, pH 7.4, containing 1% DMSO). As shown in Fig. S3, the ultraviolet absorption peak of **BMIBD** (10  $\mu$ M) was a tail peak, which was typical of Mie scattering. The average aggregate size of the probe **BMIBD** in PBS was 87 nm (Fig. S4). When Hg<sup>2+</sup> (10  $\mu$ M) was added, a new red shift peak appeared in the ultraviolet absorption spectrum, and the average particle size was 220 nm (Fig. S5). Otherwise **BMIBD** (10  $\mu$ M) showed only faint fluorescence upon excitation at 380 nm. Nevertheless, the fluorescence intensity of **BMIBD** increased gradually and the maximum fluorescent emission wavelength red-shifted from 475 nm to 495 nm after adding Hg<sup>2+</sup> from 1  $\mu$ M to 10  $\mu$ M. (Fig. 3b). The change in spectroscopy was attributed to the recovery of aldehydes after the reaction of mercury ions with **BMIBD**.

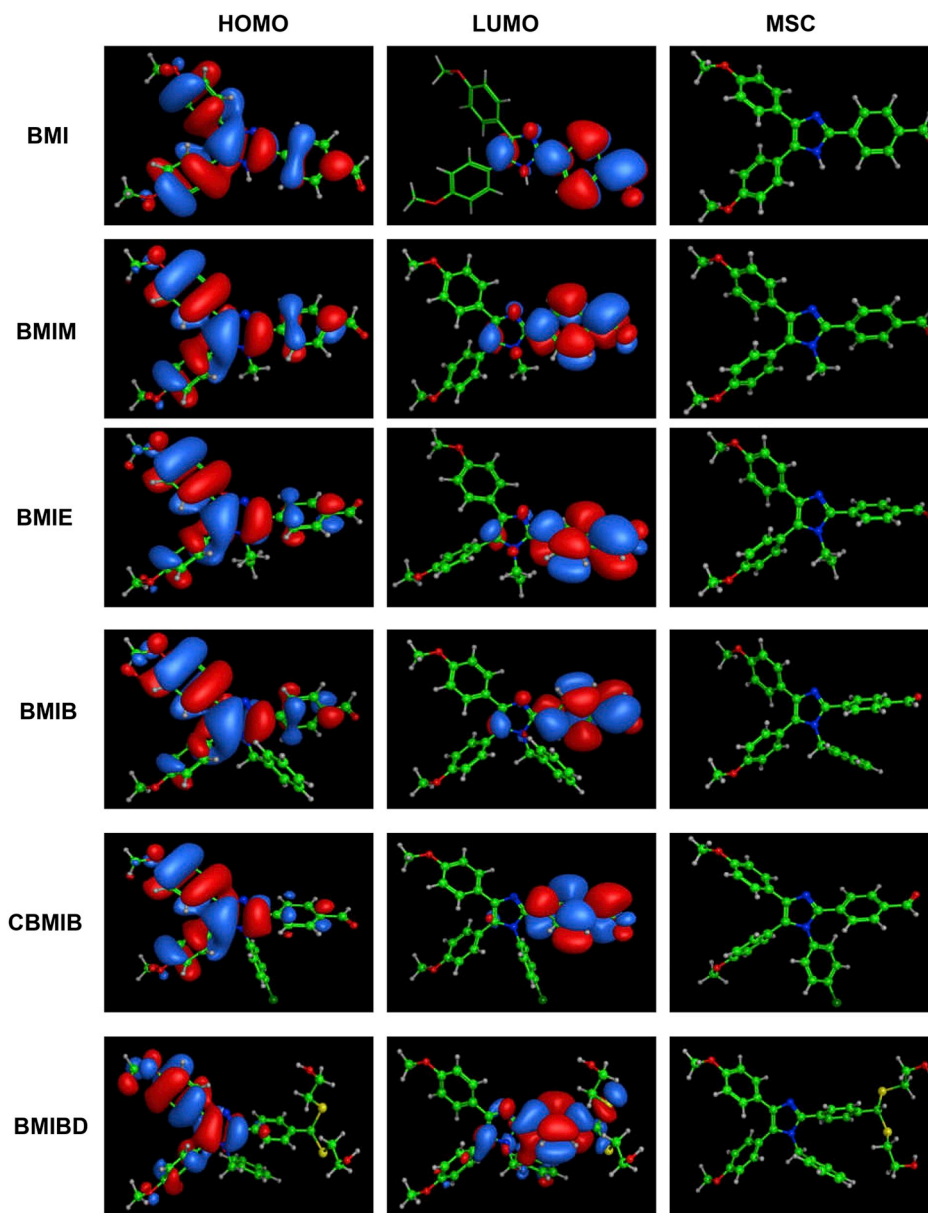


Fig. 1. Molecular orbital of the HOMO and LUMO and Most stable conformation for BMI, BMIM, BMIE, BMIB, CBMIB and BMIBD.

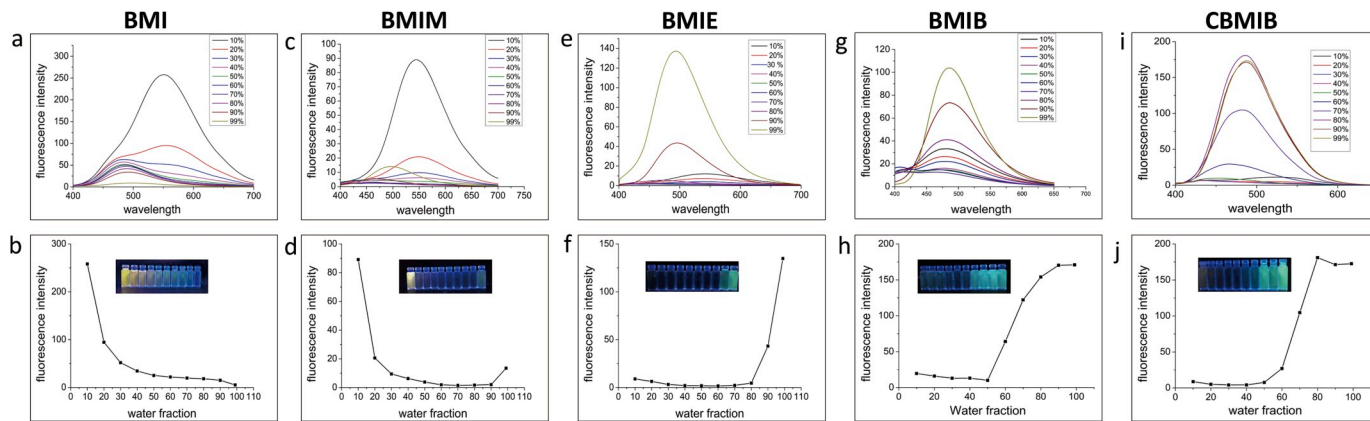
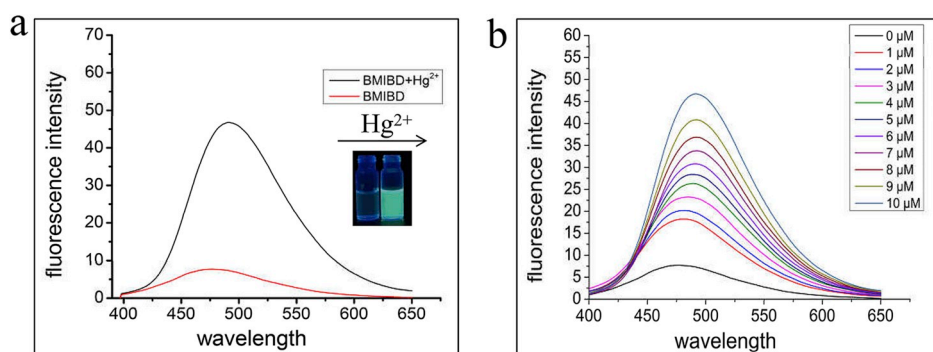
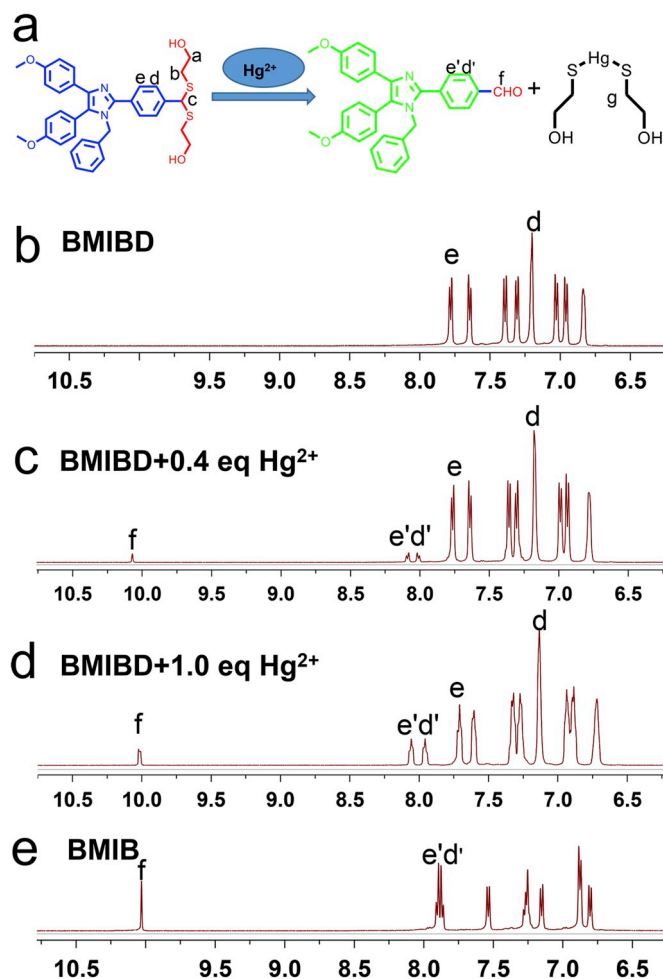


Fig. 2. (a, c, e, g, i) Fluorescence emission spectra of BMI, BMIM, BMIE, BMIB and CBMIB (10  $\mu$ M) in DMSO/water mixtures with different water fractions (fw)), (b, d, f, h, j) Fluorescence intensity versus the content of the DMSO/water mixture of BMI, BMIM, BMIE, BMIB and CBMIB (10  $\mu$ M). Inset: images of compounds with 10% to 99% water fraction in DMSO/water mixture were taken under a 365 nm hand-held UV lamp.



**Fig. 3.** (a) Fluorescence spectra of **BMIBD** (10  $\mu\text{M}$ ) without and with  $\text{Hg}^{2+}$  (10  $\mu\text{M}$ ) in PBS buffer ( $\lambda_{\text{ex}} = 380 \text{ nm}$ ). Inset picture: image of solution **BMIBD** without and with  $\text{Hg}^{2+}$ . (b) Fluorescence response of the probe **BMIBD** (10  $\mu\text{M}$ ) to  $\text{Hg}^{2+}$  at varying concentrations (0–10  $\mu\text{M}$ ) in PBS buffer ( $\lambda_{\text{ex}} = 380 \text{ nm}$ ). The incubation time of the probe with mercury ions was 20 minutes.



**Fig. 4.** (a) Proposed  $\text{Hg}^{2+}$ -induced uplung mechanism of **BMIBD**, (b, c, d)  $^1\text{H}$  NMR (500 MHz) spectra of **BMIBD** recorded upon addition of 0 equiv., 0.4 equiv. and 1.0 equiv. of  $\text{Hg}^{2+}$  in  $\text{DMSO}-d_6$ - $\text{D}_2\text{O}$  mixture, and (e)  $^1\text{H}$  NMR (500 MHz) spectra of **BMIB**.

Furthermore, in the range of 1  $\mu\text{M}$ –10  $\mu\text{M}$ , the fluorescence intensity at 495 nm exhibited a good linear relationship ( $R^2 = 0.991$ ) with the concentration of mercury ion (Fig. S6). The lowest detection limit of compound **BMIBD** for  $\text{Hg}^{2+}$  was calculated to be 0.036  $\mu\text{M}$  on basis of  $3\sigma/k$ . The amplification of fluorescence emission signal was attributed to the AIE effect thus giving the probe a relatively low detection limit for mercury ions.

Furthermore, in order to explore the optimal conditions for detection, the responsive saturation time of probe **BMIBD** to mercury ions was further studied (Fig. S7). Displayed as the result, the responsive fluorescence intensity arrived the plateau after incubation for 15 min at

37  $^\circ\text{C}$ . Moreover, the fluorescence spectra changes of the probe **BMIBD** under different pH conditions were also investigated. As shown in Fig. S8, the fluorescence emission of probe **BMIBD** was almost stable over the extensive pH range (pH = 1–11). Additionally, probe **BMIBD** with  $\text{Hg}^{2+}$  behaved as an enhanced fluorescence emission when the pH was 5–9, indicating that **BMIBD** could trace  $\text{Hg}^{2+}$  over the extensive pH range.

### 3.4. Selectivity of **BMIBD**

Selectivity is one of these crucial parameters for fluorescent probes to evaluate their applicability. As showed in Fig. S9, the obvious enhancement of fluorescence emission appeared only in the presence of  $\text{Hg}^{2+}$  (10  $\mu\text{M}$ ), while the existing of several comparative cations  $\text{Na}^+$ ,  $\text{Ca}^{2+}$ ,  $\text{Fe}^{2+}$ ,  $\text{Al}^{3+}$ ,  $\text{Mn}^{2+}$ ,  $\text{Ag}^+$ ,  $\text{Fe}^{3+}$ ,  $\text{Cr}^{3+}$ ,  $\text{Cd}^{2+}$ ,  $\text{K}^+$ ,  $\text{Mg}^{2+}$ ,  $\text{Zn}^{2+}$ ,  $\text{Co}^{2+}$  (100  $\mu\text{M}$ ) exhibited a negligible response. Probe **BMIBD** showed a 4–5 folds more obvious response toward  $\text{Hg}^{2+}$  than other cations. The results showed probe **BMIBD** exhibited superb selectivity for mercury ions from other cations.

### 3.5. Recovery test of $\text{Hg}^{2+}$ in real samples

Due to the excellent performance of the probe in terms of selectivity and sensitivity, **BMIBD** was further applied for detecting  $\text{Hg}^{2+}$  in actual environmental samples. As shown in Fig. S10, fluorescence emission spectra and quantitative standard curves at different concentrations were examined. Table S1 showed that the recovery of mercury ions in the samples was between 94.5% and 101.8% while the RSD was also less than 5%.

### 3.6. POCT for detecting $\text{Hg}^{2+}$

After gaining these inspiring results in the above experiments, the detection of  $\text{Hg}^{2+}$  ion was further carried out in the solid state. A solution of 400  $\mu\text{M}$  probe **BMIBD** in THF was adsorbed onto the polyamide film which showed nearly no emission. After the addition of mercury ions in different concentration, the test paper became strongly emissive (Fig. S11). Further, the emission was positively correlated to the concentration of  $\text{Hg}^{2+}$  ions, the more  $\text{Hg}^{2+}$  ions, the higher fluorescent intensity. The result has shown that our probe **BMIBD** possessed great potential in the test paper.

### 3.7. The mechanism for detecting $\text{Hg}^{2+}$

To verify the mechanism of the fluorescent probe for detection of mercury ions,  $^1\text{H}$  NMR titration experiment was implemented in the absence and presence of  $\text{Hg}^{2+}$ . As shown in Fig. 4d, after the addition of 1.0 eq.  $\text{Hg}^{2+}$  to the **BMIBD** in  $\text{DMSO}-d_6$ - $\text{D}_2\text{O}$  (5/1, v/v), a new aldehyde-based signal peak began to appear at a chemical shift of 10.1 ppm, and a signal peak of the methylene group attached to the sulfhydryl group in the mercaptoethanol also could be observed. At the same time,

the intensity of the signal peak of the methine group attached to the sulfur atom in **BMIBD** was reduced (Fig. S12). Furthermore, mass spectrometry was used to verify the response mechanism of **BMIBD** to  $\text{Hg}^{2+}$ . As seen in Fig. S13, the peak of  $m/z$  [ $\text{BMIB} + \text{H}$ ] $^{+}$  appeared in the MS spectrum after the addition of mercury ions. Based on these results, we speculated the mechanism of the probe response in which mercury ions induced the hydrolysis of **BMIBD** to produce **BMIB** exhibiting the enhanced fluorescence emission via the enhanced ICT effect and the fluorescent signal amplification of AIE effect (Scheme S2).

### 3.8. Cytotoxicity examination

The cytotoxicity of **BMIBD** was evaluated by the MTT assay. As shown in Fig. S14, even if the concentration of the probe **BMIBD** reached 10  $\mu\text{M}$ , the cell viability still maintained 90%, indicating that the probe **BMIBD** had good biocompatibility even at high concentration.

### 3.9. Imaging of $\text{Hg}^{2+}$ in living cells

Owing to the low cytotoxicity and excellent response to mercury ion in aqueous condition, the imaging ability of **BMIBD** for mercury ion in living cells was evaluated. As shown in Fig. 5b, in the absence of  $\text{Hg}^{2+}$ , no fluorescence was observed under the green channel. Once addition of mercury ion (5  $\mu\text{M}$  or 10  $\mu\text{M}$ ), the strong green fluorescence emission in the living cells appeared. It's worth noting that as the concentration of mercury ions increased, the fluorescence emission intensity was enhanced as well (Fig. 5e and h). It could be seen from the merged pictures that the fluorescence emission was mainly distributed in the cytoplasm (Fig. 5f and i), which illustrated that **BMIBD** had a good ability to pass through the cell membrane. These results suggested that the fluorescent probe **BMIBD** allowed imaging of  $\text{Hg}^{2+}$  in living cells with the superior characteristics of non-invasive and on-site.

## 4. Conclusions

Based on the steric effect of CFG on the imidazolium fluorophore, we introduced various CFGs on the imidazole ring to investigate the

effect of different sterically hindered groups and developed a series of AIE fluorophores. We have successfully synthesized and analysed a series of imidazolium derivatives with a branched chain or a bulky ring on the imidazole ring based on the triaryl imidazole. The experimental results showed that CFG not only played a crucial role in the restriction of intramolecular rotation in the aggregate state, but also affected the coplanarity of molecules. Due to the influence of these factors, the fluorophore originally with the ACQ effect was converted into a fluorophore with the AIE effect. Accordingly, we elaborately selected **BMIB** with excellent AIE property to develop a fluorescent molecular probe **BMIBD** to detect mercury ion. The responsive mechanism of the probe was proved by  $^1\text{H}$  NMR titration experiments and mass spectrometry. The probe **BMIBD** exhibited favourable water solubility, high selectivity and sensitivity, good linearity and superior stability over a wide pH range of 4–9. Furthermore, **BMIBD** was applied for detecting mercury ion in real water samples, POCT and imaging of mercury ion in living cells. Owing to its favourable biocompatibility, non-invasive and on-site imaging, **BMIBD** has great potential in the detection of mercury ions in environmental and biological samples.

### Conflicts of interest

There are no conflicts to declare.

### Acknowledgements

We are grateful for the financial supports from National Natural Science Foundation of China (81671756), Key Research Project of Science and Technology Foundation of Hunan Province (2017SK2093) and Changsha (kq1801063), Hunan Provincial Innovation Foundation For Postgraduate (CX20190243), and the Fundamental Research Funds for the Central Universities of Central South University (2019zzts187). We thank all members of High-Resolution Mass Spectrometry Laboratory of Advanced Research Center, Central South University for the LC-MS experiments. We also acknowledge the NMR measurements by the Modern Analysis and Testing Center of CSU and department of pharmacy at Xiangya Hospital, Central South University.

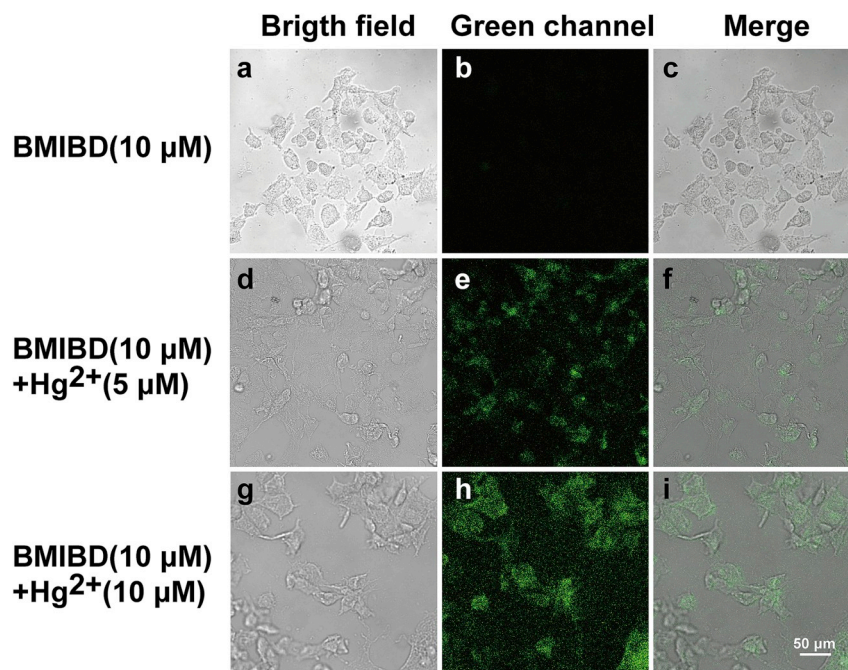


Fig. 5. Fluorescence imaging experiment of MDA-MB-231 stained with 10  $\mu\text{M}$  **BMIBD** for 30 min without and with various concentrations of  $\text{Hg}^{2+}$  (5  $\mu\text{M}$  and 10  $\mu\text{M}$ ) at 37  $^{\circ}\text{C}$  (fluorescence confocal microscope). (a, d, g) Bright field; (b, e, h) green channel; (c, f, i) merged images.

## Appendix A. Supplementary data

Supplementary data to this article can be found online at <https://doi.org/10.1016/j.dyepig.2019.107830>.

## References

- [1] Liang J, Tang B, Liu B. Specific light-up bioprobes based on AIEgen conjugates. *Chem Soc Rev* 2015;44:2798–811.
- [2] Kolanowski JL, Liu F, New EJ. Fluorescent probes for the simultaneous detection of multiple analytes in biology. *Chem Soc Rev* 2018;47:195–208.
- [3] Wu D, Sedgwick AC, Gunnlaugsson T, et al. Fluorescent chemosensors: the past, present and future. *Chem Soc Rev* 2017;46:7105–23.
- [4] Li SW, Ling X, Lin YH, et al. In situ generation of photoactivatable aggregation-induced emission probes for organelle-specific imaging. *Chem Sci* 2018;9:5730–5.
- [5] Meher N, Iyer PK. Spontaneously self-assembled naphthalimide nanosheets: aggregation-induced emission and unveiling a-PET for sensitive detection of organic volatile contaminants in water. *Angew Chem Int Ed* 2018;57:8488–92.
- [6] Yang L, Ye P, Li WQ, et al. Uncommon aggregation-induced emission molecular materials with highly planar conformations. *Adv Opt Mater* 2018;6:1701394.
- [7] Bu LL, Chen JQ, Wei XD, et al. An AIE and ICT based NIR fluorescent probe for cysteine and homocysteine. *Dyes Pigments* 2017;136:724–31.
- [8] Mei J, Hong YN, Lam J, et al. Aggregation-Induced emission: the whole is more brilliant than the parts. *Adv Mater* 2014;26:5429–79.
- [9] Xue MJ, Wang H, Chen J, et al. Ratiometric fluorescent sensing of endogenous hypochlorous acid in lysosomes using AIE-based polymeric nanoprobe. *Sens Actuators B Chem* 2019;282:1–8.
- [10] Jiang GY, Zeng GJ, Zhu WP, et al. A selective and light-up fluorescent probe for beta-galactosidase activity detection and imaging in living cells based on an AIE tetraphenylethylene derivative. *Chem Commun* 2017;53:4505–8.
- [11] Feng GX, Liu B. Aggregation-induced emission (AIE) dots: emerging theranostic nanolights. *Acc Chem Res* 2018;51:1404–14.
- [12] Gao M, Su HF, Li SW, et al. An easily accessible aggregation-induced emission probe for lipid droplet-specific imaging and movement tracking. *Chem Commun* 2017;53:921–4.
- [13] La DD, Bhosale SV, Jones LA, Bhosale SV. Tetraphenylethylene-based AIE-active probes for sensing applications. *ACS Appl Mater Interfaces* 2018;10:12189–216.
- [14] Yi XY, Li J, Zhu ZP, et al. In vivo cancer research using aggregation-induced emission organic nanoparticles. *Drug Discov Today* 2017;22:1412–20.
- [15] Chen YC, Lam J, Kwok R, Liu B, Tang BZ. Aggregation-induced emission: Fundamental understanding and future developments. *Mater Horiz* 2019;6:428–33.
- [16] Gao H, Zhao X, Chen SJ. AIEgen-based fluorescent nanomaterials: fabrication and biological applications. *Molecules* 2018;23:419.
- [17] Gopikrishna P, Meher N, Iyer PK. Functional 1,8-naphthalimide AIE/AIEEgens: recent advances and prospects. *ACS Appl Mater Interfaces* 2018;10:12081–111.
- [18] Mei J, Huang YH, Tian H. Progress and trends in AIE-based bioprobes: a brief overview. *ACS Appl Mater Interfaces* 2018;10:12217–61.
- [19] Zhang YX, Wang YF, Wang JJ, Liang XJ. Improved pharmaceutical research and development with AIE-based nanostructures. *Mater Horiz* 2018;5:799–812.
- [20] Shi J, Li Y, Li QQ, Li Z. Enzyme-responsive bioprobes based on the mechanism of aggregation-induced emission. *ACS Appl Mater Interfaces* 2018;10:12278–94.
- [21] Hu JY, Liu R, Zhai SL, et al. AIE-active molecule-based self-assembled nano-fibrous films for sensitive detection of volatile organic amines. *J Mater Chem C* 2017;5:11781–9.
- [22] Li N, Feng HL, Gong Q, et al. BINOL-based chiral aggregation-induced emission luminogens and their application in detecting copper(II) ions in aqueous media. *J Mater Chem C* 2015;3:11458–63.
- [23] Meher N, Panda S, Kumar S, Iyer PK. Aldehyde group driven aggregation-induced enhanced emission in naphthalimides and its application for ultradetection of hydrazine on multiple platforms. *Chem Sci* 2018;9:3978–85.
- [24] Mei J, Leung NLC, Kwok PTK, Lam JWY, Tang BZ. Aggregation-induced emission: together we shine, united we soar. *Chem Rev* 2015;115:11718–940.
- [25] Gao T, Cao XZ, Bi AY, et al. An Aza-Cope mediated fluorescent probe based on aggregation-induced emission for highly selective and sensitive detection of formaldehyde in living cells and tissues. *Sens Actuators B Chem* 2018;273:1139–45.
- [26] Gao T, Zeng HL, Xu H, et al. Novel self-assembled organic nanoprobe for molecular imaging and treatment of gram-positive bacterial infection. *Theranostics* 2018;8:1911–22.
- [27] Lan LX, Niu QF, Li TD. A highly selective colorimetric and ratiometric fluorescent probe for instantaneous sensing of Hg<sup>2+</sup> in water, soil and seafood and its application on test strips. *Anal Chim Acta* 2018;1023:105–14.
- [28] Erdemir S, Kocycigit O. A novel dye based on phenolphthalein-fluorescein as a fluorescent probe for the dual-channel detection of Hg<sup>2+</sup> and Zn<sup>2+</sup>. *Dyes Pigments* 2017;145:72–9.
- [29] Gao YY, Ma TT, Ou ZZ, et al. Highly sensitive and selective turn-on fluorescent chemosensors for Hg<sup>2+</sup> based on thioacetal modified pyrene. *Talanta* 2018;178:663–9.
- [30] Wu CY, Peng X, Lu QJ, et al. Ultrasensitive silicon nanoparticle ratiometric fluorescence determination of mercury(II). *Anal Lett* 2018;51:1013–28.
- [31] Bhatta SR, Mondal B, Vijaykumar G, Thakur A. ICT-isomerization-induced turn-on fluorescence probe with a large emission shift for mercury ion: application in combinational molecular logic. *Inorg Chem* 2017;56:11577–90.
- [32] Zhou Y, He XF, Chen H, et al. An ESIPT/ICT modulation based ratiometric fluorescent probe for sensitive and selective sensing Hg<sup>2+</sup>. *Sens Actuators B Chem* 2017;247:626–31.
- [33] Feng YS, Kuai ZY, Song Y, et al. A novel "turn-on" thiooxofluorescein-based colorimetric and fluorescent sensor for Hg<sup>2+</sup> and its application in living cells. *Talanta* 2017;170:103–10.
- [34] Ghasemi F, Hormozi-Nezhad MR, Mahmoudi M. A new strategy to design colorful ratiometric probes and its application to fluorescent detection of Hg(II). *Sens Actuators B Chem* 2018;259:894–9.
- [35] Chen BY, Kuo CC, Cho CJ, Liang FC, Jeng RJ. Novel fluorescent chemosensory filter membranes composed of electrospun nanofibers with ultra-selective and reversible pH and Hg<sup>2+</sup> sensing characteristics. *Dyes Pigments* 2017;143:129–42.
- [36] Zhao JJ, Huang MJ, Zhang LL, et al. Unique approach to develop carbon dot-based nanohybrid Near-Infrared ratiometric fluorescent sensor for the detection of mercury ions. *Anal Chem* 2017;89:8044–9.
- [37] Xu D, Tang LJ, Tian MY, He P, Yan XM. A benzothiazole-based fluorescent probe for Hg<sup>2+</sup> recognition utilizing ESIPT coupled AIE characteristics. *Tetrahedron Lett* 2017;58:3654–7.
- [38] Mahato P, Saha S, Das P, Agarwalla H, Das A. An overview of the recent developments on Hg<sup>2+</sup> recognition. *RSC Adv* 2014;4:36140–74.
- [39] Inamuddin, Khan SA, Siddiqui WA, Khan AA. Synthesis, characterization and ion-exchange properties of a new and novel 'organic-inorganic' hybrid cation-exchanger: nylon-6,6, Zr(IV) phosphate. *Talanta* 2007;71:841–7.
- [40] Huang LY, Yang ZT, Zhou ZL, et al. A dual colorimetric and near-infrared fluorescent turn-on probe for Hg<sup>2+</sup> detection and its applications. *Dyes Pigments* 2019;163:118–25.
- [41] Chan J, Dodani SC, Chang CJ. Reaction-based small-molecule fluorescent probes for chemoselective bioimaging. *Nat Chem* 2012;4:973–84.
- [42] Xu J, Li HL, Chen YC, et al. A novel fluorescent probe for Hg<sup>2+</sup> detection in a wide pH range and its application in living cell imaging. *Anal Methods* 2018;10:5554–8.
- [43] Song F, Yang C, Shao XT, et al. A reversible "turn-off-on" fluorescent probe for real-time visualization of mercury(II) in environmental samples and its biological applications. *Dyes Pigments* 2019;165:444–50.
- [44] Peng D, Zhang L, Liang RP, Qiu JD. Rapid detection of mercury ions based on nitrogen-doped graphene quantum dots accelerating formation of manganese porphyrin. *ACS Sens* 2018;3:1040–7.
- [45] Wang DM, Gai QQ, Huang RF, Zheng XW. Label-free electrochemiluminescence assay for aqueous Hg<sup>2+</sup> through oligonucleotide mediated assembly of gold nanoparticles. *Biosens Bioelectron* 2017;98:134–9.
- [46] Zhang XL, Xiao Y, Qian XH. A ratiometric fluorescent probe based on FRET for imaging Hg<sup>2+</sup> ions in living cells. *Angew Chem Int Ed* 2008;47:8025–9.
- [47] Cao T, Teng ZD, Gong DY, et al. A ratiometric fluorescent probe for detection of endogenous and exogenous hydrogen sulfide in living cells. *Talanta* 2019;198:185–92.